

Cite this: *Environ. Sci.: Nano*, 2022, 9, 511

# Towards a broad-operation window for stable CO<sub>2</sub> electroreduction to HCOOH by a design involving upcycling electroplating sludge-derived Sn@N/P-doped carbon†

Xiaohui Zhong,<sup>a</sup> Zuqi Zhong,<sup>a</sup> Shujie Liang,<sup>a</sup> Gongchang Zeng,<sup>ID</sup><sup>a</sup>  
Shuang Cheng,<sup>ID</sup><sup>a</sup> Hong Deng,<sup>ID</sup><sup>\*ab</sup> and Zhang Lin,<sup>ID</sup><sup>ac</sup>

The electrochemical CO<sub>2</sub> reduction reaction (CO<sub>2</sub>RR) to HCOOH offers a promising strategy for a carbon-neutral cycle. Sn-Based materials have been demonstrated as applicable in extensive studies of CO<sub>2</sub>RR to HCOOH, but great challenges still remain, including the weak CO<sub>2</sub> adsorption and narrow potential window as well as low stability. Herein, we developed ultrasmall Sn nanoparticles inlaid on N/P-doped carbon (Sn@NPC) composites by an upcycling design using Sn electroplating sludge. The obtained Sn@NPC electrode exhibited a higher Faradaic efficiency of 87.93% for HCOOH at 1.05 V vs. RHE and an FE over 80% within a 500 mV broad potential window. Moreover, the Sn@NPC electrode achieved excellent long-term stability up to 105 h, which was superior to that of most Sn-based catalysts in similar systems. Density functional theory calculations demonstrated that Sn@NPC could enhance CO<sub>2</sub> adsorption, which led to stronger \*OCHO adsorption, weaker \*HCOOH adsorption and faster electron/mass transport. This work may provide a promising lead for recycling metal from electroplating sludge and for the design of efficient and stable catalysts for the CO<sub>2</sub>RR.

Received 10th October 2021,  
Accepted 14th December 2021

DOI: 10.1039/d1en00930c

rsc.li/es-nano

## Environmental significance

Excess greenhouse gases have a serious impact on climate and environmental issues. Tin-based materials represent a good electrocatalytic carbon dioxide reduction material. The declining trend in the reserves of global tin resources and the low resource-guarantee years indicate that tin production is difficult to sustain growth. However, the current tin-containing electroplating sludge is mainly landfilled, and it is not well used. In this study, the ultrasmall Sn nanoparticles inlaid on N/P-doped carbon (Sn@NPC) composite were successfully synthesized by a design involving the upcycling of Sn electroplating sludge, using bacteria as the support. The as-synthesized Sn@NPC showed excellent selectivity and stability for electrochemical reduction CO<sub>2</sub> to formic acid. This “killing two birds with one stone” strategy provides a facile approach for carbon neutrality, environmental protection and sustainable economic development.

## 1. Introduction

Since the 21st century, with the intensification of the greenhouse effect and energy crisis, converting CO<sub>2</sub> into

carbohydrates through electrocatalysis, photocatalysis and thermo-catalysis has attracted widespread attention.<sup>1–5</sup> In particular, the electrochemical CO<sub>2</sub> reduction reaction (CO<sub>2</sub>-RR) is a promising strategy for converting CO<sub>2</sub> to high-value-added chemicals.<sup>6,7</sup> However, CO<sub>2</sub> electroreduction faces two general challenges. One is that the CO<sub>2</sub> molecule is thermodynamically stable, leading to a large application potential required during the reduction process. The other is that CO<sub>2</sub>RR involves multi-electron-transfer pathways, which limits the selectivity of the product and is accompanied by a competitive process of the hydrogen evolution reaction (HER).<sup>8,9</sup> Among these CO<sub>2</sub> reduction products, HCOOH, as one of the high-value-added chemicals produced, possesses potential applications in industrial synthesis. Importantly, the electrochemical reduction of CO<sub>2</sub> to HCOOH is a two-electron process with high product selectivity, compared to

<sup>a</sup> School of Environment and Energy, Guangdong Provincial Key Laboratory of Solid Wastes Pollution Control and Recycling, The Key Laboratory of Pollution Control and Ecosystem Restoration in Industry Clusters (Ministry of Education), South China University of Technology, Guangzhou, Guangdong 510006, China.  
E-mail: dengh2016@scut.edu.cn

<sup>b</sup> Guangdong Engineering and Technology Research Center for Environmental Nanomaterials, South China University of Technology, Guangzhou, Guangdong 510006, China

<sup>c</sup> Chinese National Engineering Research Center for Control & Treatment of Heavy Metal Pollution, School of Metallurgy and Environment, Central South University, Changsha 410083, China

† Electronic supplementary information (ESI) available. See DOI: 10.1039/d1en00930c

other conversion ways aiming for high-value-added chemicals, and is considered one of the most promising and economically viable reactions.<sup>10–12</sup>

The core of the CO<sub>2</sub>RR to HCOOH lies in the design of high-efficiency electrocatalysts. Among those electrocatalysts, noble metals, such as Au,<sup>13,14</sup> Ag,<sup>15,16</sup> and even some single-atom catalysts<sup>17,18</sup> are usually preferred for the high selectivity of CO. For the CO<sub>2</sub>RR to HCOOH, Sn,<sup>19,20</sup> Bi,<sup>21,22</sup> Pb,<sup>23,24</sup> In,<sup>25,26</sup> Pd (ref. 27 and 28) and some heteroatom-doped carbon-based materials<sup>29,30</sup> have better catalytic performance. In particular, Sn-based materials are the most attractive electrocatalysts due to their good activity, high selectivity and non-toxicity. In 1994, Hori *et al.* first reported a high HCOOH selectivity (88.4%) for the electrochemical CO<sub>2</sub> reduction of monolithic Sn in 0.1 M KHCO<sub>3</sub> solution.<sup>31</sup> Spurgeon and co-workers showed that a SnO<sub>2</sub> porous nanowire catalyst could attain a maximum FE<sub>HCOOH</sub> value of 80% at –0.8 V *vs.* RHE.<sup>32</sup> Wang *et al.* prepared Sn-based catalysts by an electrodeposition method, and demonstrated the maximum Faradaic efficiency for HCOOH of 91% at –1.4 V *vs.* SCE.<sup>33</sup> However, these individual materials have a narrow potential window for relatively high HCOOH selectivity, and the stability of CO<sub>2</sub>RR is typically a bitter disappointment with a significant decrease in activity after a few hours.<sup>32,34</sup> To overcome these difficulties, measures such as reducing the catalysts size, doping, introducing vacancies, and binding with a carbon support have been used to increase the active sites and enhance the electron-transfer ability or CO<sub>2</sub> adsorption capacity, thus further effectively improving the CO<sub>2</sub>RR selectivity and stability. For example, Xie *et al.* demonstrated that metallic Sn quantum sheets confined in graphene was conducive to enhancing the CO<sub>2</sub>RR to HCOOH activity and stability, with a maximum Faradaic efficiency of 89% and long-term stability over 50 h.<sup>35</sup> Interestingly, Ohto *et al.* recently reported that the oxidized functional groups on the reduced graphene oxide could provide CO<sub>2</sub> adsorption sites for adjacent Sn surfaces and thus promote the \*OCHO intermediate generation, and the Faradaic efficiency of HCOOH was as high as 98 ± 0.7% at –820 mV *vs.* RHE.<sup>36</sup> These studies showed that carbon materials could serve as a kind of ideal support, which can assist in enhancing the CO<sub>2</sub>RR performance of Sn-based catalysts in different aspects.

Given the foregoing discussion and the resource scarcity of Sn, recovering Sn metal from solid waste to construct Sn-based catalysts is an economically feasible method with significant environmental importance and great potential for industrial commercialization. Herein, ultrasmall Sn nanoparticles were inlaid on N/P-doped carbon (Sn@NPC) electrocatalytic material by recycling the Sn metal from electroplating sludge, using bacteria as the support, which allowed constructing a special structure followed by *in situ* heteroatom doping. The prepared Sn@NPC electrode exhibited a high Faradaic efficiency of 87.93% for HCOOH at 1.05 V *vs.* RHE and the FE was over 80% within a 500 mV potential window. More importantly, the electrode had a

satisfactory electrochemical stability of over 105 h with a relatively high FE<sub>HCOOH</sub> (~85%) and reduction current density (~8.0 mA cm<sup>–2</sup>). Density functional theory (DFT) calculations and *in situ* Raman spectroscopic studies demonstrated that N/P-doped carbon could enhance the adsorption of CO<sub>2</sub>, which then supplied sufficient feedstock for the neighbouring Sn surface to efficiently promote the \*OCHO intermediate generation. In addition, the strong binding strength of \*OCHO and weak adsorption energies for \*HCOOH further explained the reason why Sn@NPC favoured HCOOH production in a wide potential window and the long-term stability. These encouraging results provide a new idea for the high-value utilization of waste and the design of high-efficiency CO<sub>2</sub>RR electrocatalysts.

## 2. Experimental section

### 2.1 Samples preparation

**Culture of bacteria.** Sodium chloride (0.5 g), yeast powder (0.5 g), tryptone (1 g) and glucose (1 g) were added to 100 mL deionized water, with consecutive stirring until the solution was clear. Subsequently, *Bacillus subtilis* (BS) were cultured in the above medium solution at 35 °C for 20 h. Next, the obtained BS was collected by centrifugation and washed three times with deionized water for subsequent use.

**Pretreatment of the electroplating sludge.** The Sn electroplating sludge (Sn, 58.75 wt%, from Fujian Zhongrida Metal Co., Ltd., Table S2†) was first dried at 90 °C overnight and then ground to fine powder. Next, 0.5 g powder was added into 5 mL hydrochloric acid solution, and then the Sn electroplating sludge extracting solution was obtained after ultrasonic stirring for 1 hour and filtration.

**Synthesis of Sn@NPC composites.** First, the sludge extracting solution was diluted into 100 mL. Then, 10 g *Bacillus subtilis* was put into the diluted solution and stirred at room temperature for 24 h. After that, the mixed solution was centrifugally washed to obtain the Sn@BS precursor. Finally, the lyophilized precursor was annealed at 700 °C for 30 min under 5% H<sub>2</sub>/Ar condition with a heating rate of 10 °C min<sup>–1</sup> to obtain the Sn@NPC composites. The pristine N/P-doped carbon (NPC) was prepared using the same method without Sn electroplating sludge extracting solution. The Sn@BS precursor was calcined to synthesize the control samples of Sn@NPC (700 °C) at different temperatures of 500 °C, 600 °C, and 800 °C (Fig. S1 and S2†). The adsorption of Sn by *Bacillus subtilis* directly affected the content of Sn in the Sn@NPC composites, and samples with different masses of Sn electroplating sludge (0.3 g named as Sn@NPC-A, 0.4 g named as Sn@NPC-B) were also synthesized. According to the inductively coupled plasma optical emission spectrometry (ICP-OES) analysis (Table S3†), the adsorption capacity of *Bacillus subtilis* for Sn ions was basically saturated at 0.4–0.5 g. Subsequent linear sweep voltammetry (LSV) and Faraday efficiency tests showed that there was no significant improvement in the activity of CO<sub>2</sub> reduction when the concentration of Sn was over 2350 ppm (Fig. S3†).

**Preparation of Sn particles.** Typically, 50 mL 0.1 M tin(IV) chloride pentahydrate ( $\text{SnCl}_4 \cdot 5\text{H}_2\text{O}$ , 98%, Aladdin) solution was prepared. Next, excess 0.2 M sodium borohydride ( $\text{NaBH}_4$ , 98%, Aladdin) solution was slowly added and continuously stirred for 5 min. The grey precipitate was obtained, filtered, washed three times with deionized water and finally dried out at 70 °C under vacuum. The morphology and crystalline structure were characterized, as shown in Fig. S4.†

## 2.2 Material characterization

The morphology of the as-prepared samples was observed by field emission scanning electron microscopy (FE-SEM, SU8100, Hitachi) with a 10 kV accelerating voltage. The detailed microstructure and element analysis were characterized by a high-resolution transmission electron microscopy instrument (HR-TEM, JEOL-2100F) equipped with an energy dispersive X-ray spectroscopy (EDS) system. The crystal structure of the samples was examined by powder X-ray diffraction (XRD) on a Bruker D8 Advance Powder diffractometer with  $\text{Cu-K}\alpha$  radiation (40 kV, 40 mA). The surface chemical compositions of the composites were analyzed using X-ray photoelectron spectroscopy (XPS, Thermo Fisher Scientific, K-alpha+) with the reference C1s peak (284.8 eV). Raman spectra (*in situ* Raman) were obtained using a laser Raman spectrometer (LabRamHR, HORIBA Jobin Yvon. Co., France) with a 532 nm excitation laser. The Sn content of Sn@NPC composites was determined by inductively coupled plasma optical emission spectrometry (ICP-OES, Avio 200, PerkinElmer). The Fourier transform infrared (FTIR) spectra were recorded on a NICOLET FTIR spectrometer with KBr pellets (Thermo Scientific, USA). The  $\text{CO}_2$  adsorption isotherms were collected by an automatic microporous physical and chemical gas adsorption analyzer (ASAP 2020) at 298 K.

## 2.3 Electrochemical measurements

All the electrochemical measurements were carried out on a typical three-electrode H-type cell system using an electrochemical workstation (CHI 660E). A saturated calomel electrode ( $\text{Hg}/\text{Hg}_2\text{Cl}_2/\text{KCl}$ , SCE) and a platinum net ( $1 \times 1 \text{ cm}^2$ , 99.99%) were used as the reference electrode and the counter electrode, respectively. The working electrode was prepared in the typical procedure with 200  $\mu\text{L}$  of the homogeneous ink, which was prepared by dispersing 3 mg sample in 1 mL water–ethanol solution ( $v/v = 1:1$ ) with 40  $\mu\text{L}$  5 wt% Nafion solution, then dropped on carbon cloth ( $\sim 1 \text{ cm} \times 1 \text{ cm}$ ). All the measured SCE reference electrode potentials were calibrated to the reversible hydrogen electrode (RHE) by using the Nernst equation:

$$E_{\text{RHE}} = E_{\text{SCE}} + 0.0591 \times \text{pH} + 0.241 \quad (1)$$

The  $\text{CO}_2$ -saturated or Ar-saturated 0.1 M  $\text{KHCO}_3$  aqueous solution (pH = 6.76 for  $\text{CO}_2$ -saturation and pH = 8.40 for Ar-

saturation) was used as the electrolyte for the  $\text{CO}_2$ RR measurements. The pH of the electrolyte was checked using a benchtop pH meter (PHS-3C, Shanghai INESA Scientific Instrument). The  $\text{CO}_2$  gas flow was controlled at 20 sccm using a mass flow controller. All the linear sweep voltammetry (LSV) measurements were recorded at a 10  $\text{mV s}^{-1}$  scan rate to examine the electrochemical activity in  $\text{CO}_2$ - or Ar-saturated 0.1 M  $\text{KHCO}_3$  aqueous solution, and the Tafel slopes were based on an analysis of these data. Electrochemical impedance spectroscopy (EIS) was carried out at 1.0 V vs. RHE in a frequency range of 100 000–0.1 Hz with an amplitude of 5 mV. To calculate the electrochemically active surface area (ECSA) of the working electrodes, the double-layer capacitance ( $C_{\text{dl}}$ ) was determined by cyclic voltammograms (CV) in a non-Faradaic current response region of  $-0.05$ – $0.5$  V vs. SCE at scan rates of 2, 4, 6, 8, and 10  $\text{mV s}^{-1}$ . The current difference ( $\Delta j$ ) between the anodic current ( $j_{\text{a}}$ ) and cathodic current ( $j_{\text{c}}$ ) at 0 V vs. SCE was plotted against the scan rate, and the linear slope was twice that of  $C_{\text{dl}}$ .<sup>37,38</sup> The ECSA was calculated according to the equation:

$$\text{ECSA} = R_{\text{f}}S \quad (2)$$

$$R_{\text{f}} = \frac{C_{\text{dl}}}{C_{\text{s}}} \quad (3)$$

where  $R_{\text{f}}$  is the roughness factor,  $S$  is the real geometric area of the working electrode (In this work,  $S = 1 \text{ cm}^2$ ), and  $C_{\text{s}}$  is the specific capacitance of the sample. Considering the practical problems in this system, it is not practical for the electrodes to measure the  $C_{\text{s}}$ .<sup>39</sup> Therefore, the  $C_{\text{s}}$  of the carbon cloth substrate in the same electrolyte was measured to replace the  $C_{\text{s}}$  of the sample.

The turnover frequency (TOF) is defined as the number of turnovers per active sites per second. The TOF for the  $\text{CO}_2$ RR to HCOOH was calculated based on the 2-electron pathway using the following equation:<sup>40</sup>

$$\text{TOF} (\text{h}^{-1}) = \frac{J_{\text{HCOOH}}/2F}{m\omega/M} \times 3600 \quad (4)$$

where  $J_{\text{HCOOH}}$  is the current density of HCOOH (A),  $F$  is the Faraday constant (96 485 C/mol),  $m$  is the mass of the loaded Sn@NPC (or Sn particles) in the electrode ( $g$ ),  $\omega$  is the mass fraction of tin in the as-prepared samples, and  $M$  is the atomic mass of Sn.

## 2.4 Products analysis

The gas products were detected and quantified by a gas chromatograph (Shimadzu, GC-2014) equipped with a thermal conductivity detector (TCD) for  $\text{H}_2$  and a flame ionization detector (FID) for CO quantification. High-purity argon (99.9999%) was applied as the carrier gas. The Faradaic efficiency (FE) of the gas products was calculated as follows equation:

$$FE(\%) = \frac{Q_{\text{product}}}{Q_{\text{total}}} = \frac{C_{\text{product}} \times V_{\text{CO}_2} \times n \times F \times P}{R \times T \times J} \quad (5)$$

where  $C_{\text{product}}$  is the volume concentration of CO or H<sub>2</sub> product (ppm),  $V_{\text{CO}_2}$  is the flow rate of CO<sub>2</sub> (20 sccm),  $n$  is the number of transferred electrons for product,  $F$  is the Faraday constant (96 485 C/mol),  $P$  is the standard atmospheric pressure (101 325 Pa),  $R$  is the gas constant (8.314),  $T$  is the temperature for testing (K), and  $J$  is the reduction current at a specific applied potential.

The liquid products were identified by <sup>1</sup>H nuclear magnetic resonance (<sup>1</sup>H-NMR, Bruker BioSpin GmbH) in which 500 μL electrolyte was mixed with 100 μL deuterated water (D<sub>2</sub>O) and 5 mg phenol (Sigma, 99.99%) was added as an internal standard. The <sup>1</sup>H spectrum peak of HCOOH was at ~8.3 and that of phenol was at ~7.2. The Faradaic efficiency of HCOOH can be calculated as follows:

$$FE(\%) = \frac{Q_{\text{HCOOH}}}{Q_{\text{total}}} = \frac{2 \times C_{\text{HCOOH}} \times V \times F}{J \times t} \quad (6)$$

where  $C_{\text{HCOOH}}$  stands for the concentration of HCOOH after electrolysis (ppm),  $V$  is the volume of electrolyte on the side of the working cell (mL),  $F$  is the Faraday constant (96 485 C/

mol), and  $J$  and  $t$  are the reduction current and electrolysis time at a specific applied potential.

## 2.5 DFT calculations

All the first-principles calculations were performed within the Vienna *ab initio* simulation package (VASP) based on density functional theory (DFT). The projector augmented wave (PAW) potentials were used to deal with the electronic exchange-correlation interaction along with the GGA functional in the parameterization of the Perdew, Burke, and Ernzerhof (PBE) pseudopotential. A plane wave representation for the wave function with a cut off energy of 450 eV was applied. Geometry optimizations were performed using conjugate gradient minimization until all the forces acting on the ions were less than 0.02 eV/Å per atom. A 15 Å vacuum in the  $z$  direction was used to separate the slabs. In the calculations, a  $k$ -point mesh with a spacing of *ca.* 0.03 Å<sup>-1</sup> was adopted.

## 3. Results and discussion

### 3.1 Morphology and microstructure

The Sn@NPC composites were synthesized by annealing the obtained precursors of Sn@BS at high temperature, as

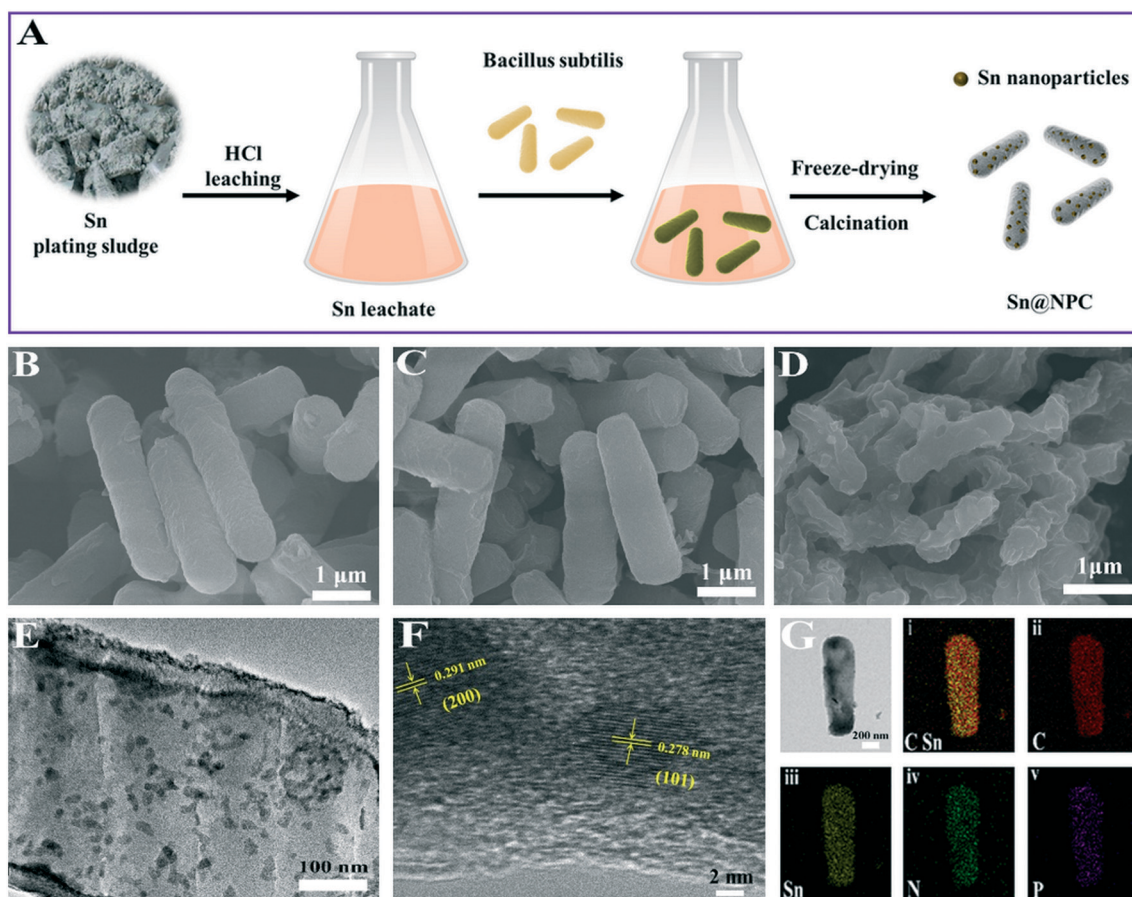


**Fig. 1** (A) Schematic description of the synthesis process for Sn@NPC composites; FE-SEM images of (B) BS, (C) Sn@BS and (D) Sn@NPC; cross-sectional TEM image at (E) lower magnification and (F) higher magnification; (G) TEM image and the corresponding EDS mapping profiles for the Sn, N, and P of the Sn@NPC composites.

presented in Fig. 1A (full details given in the Experimental section). The morphology and microstructure of the *Bacillus subtilis*, Sn@BS and Sn@NPC were observed by FE-SEM and TEM. The bacteria and Sn@BS showed a rod-like structure, with a length of  $\sim 2.5$   $\mu\text{m}$  and an average diameter of about 500 nm (Fig. 1B and C). After calcination, the morphology of the obtained Sn@NPC composites showed obvious shrinkage in comparison to the original rod-like structure, indicating that the high-temperature treatment resulted in dehydration and carbonization of the bacteria (Fig. 1D). To gain insights into the internal information on the Sn@NPC, TEM analysis was performed and clearly manifested that the ultrasmall Sn nanoparticles were homogeneously distributed on the composites (Fig. 1E). Meanwhile, the HR-TEM image revealed a set of regular lattice fringes with spacings of  $\sim 0.278$  nm and  $\sim 0.291$  nm, respectively, corresponding to the (101) and (200) crystal planes of Sn (Fig. 1F). The TEM-EDS mapping analysis of Sn, N and P further confirmed the uniform dispersion of each element in the Sn@NPC composites (Fig. 1G). These results indicated that the bacteria could be used as an exceptional substrate to prevent the agglomeration of Sn nanoparticles during the high-temperature calcination.

### 3.2 Physical and chemical properties

The crystalline structure and composition of Sn@NPC composites were confirmed by XRD and XPS. As shown in Fig. 2A, there were no obvious peaks in the XRD pattern of Sn@BS, indicating that Sn existed in the amorphous form after adsorption by *Bacillus subtilis*. After calcination, all the

diffraction peaks were perfectly assigned to the monolithic Sn (JCPDS 01-086-2264), with the two strongest peaks at  $30.7^\circ$  and  $32.0^\circ$  attributed to the exposure of (200) and (101) facets.<sup>41</sup> XPS study also revealed the presence of Sn in the Sn@NPC composites (Fig. 2B), with the asymmetry of the Sn  $3d_{5/2}$  binding energy values ( $\sim 484.97$  and  $\sim 485.86$  eV) indicating the existence of  $\text{Sn}^0$  and  $\text{Sn}^{2+}$ , in which the weak signal of  $\text{Sn}^{2+}$  might be due to the partial oxidation.<sup>42</sup> Also, in the XPS survey spectrum of Sn@NPC (Fig. S5<sup>†</sup>), the characteristic peaks of C, O, P and N were clearly observed. The two peaks located in the P 2p region were attributed to the characteristic peaks of phosphates and metaphosphates (Fig. 2C).<sup>43</sup> Besides, the N 1s spectrum could be deconvoluted into three peaks belonging to pyridinic N (398.42 eV), pyrrolic N (399.68 eV) and graphitic N (400.94 eV), respectively (Fig. 2D).<sup>44</sup> The appearance of N 1s and P 2p peaks proved that the N and P elements were successfully doped after carbonization. Such heteroatom doping may improve electron transfer and thus promote the electrochemical activity of Sn@NPC.

To further understand the origin of N and P elemental doping, FTIR was used to verify the interaction between the functional groups of *Bacillus subtilis* and Sn metal ions during the adsorption process. In Fig. 2E, peaks related to protein could be clearly observed at  $\sim 1650$ ,  $\sim 1500$  and  $\sim 1248$   $\text{cm}^{-1}$  (amide I, II and III, respectively), with additional peaks related to phosphates observed at around  $960$   $\text{cm}^{-1}$ , which provided a source for the N and P elements.<sup>45,46</sup> After adsorption and subsequent calcination, a new peak around  $580$   $\text{cm}^{-1}$  appeared for Sn@NPC composites, which belonged to the stretching vibration of the Sn–O bond.<sup>45,47</sup> Meanwhile,

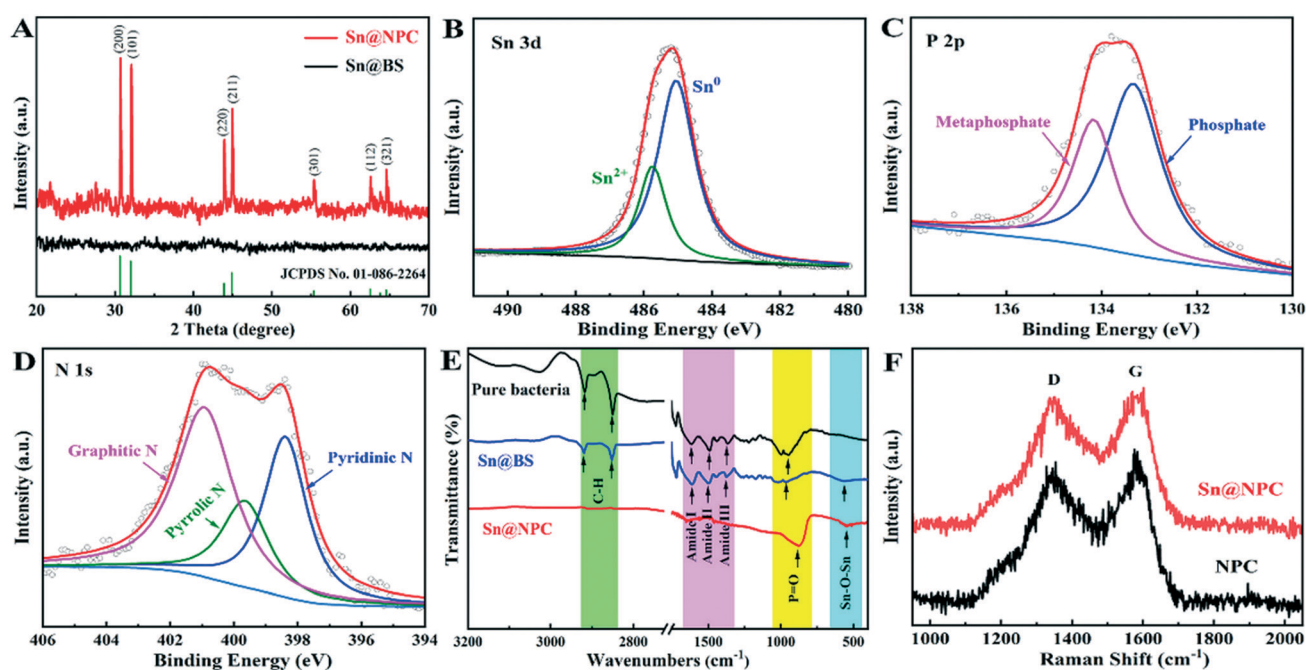


Fig. 2 (A) XRD pattern of Sn@BS and Sn@NPC; high-resolution XPS spectra of (B) Sn 3d, (C) P 2p and (D) N 1s collected from the Sn@NPC composites; (E) FTIR spectra of pure bacteria, Sn@BS and Sn@NPC; (F) Raman spectra of NPC and Sn@NPC.

the disappearance of the protein band indicated the bacteria had been completely carbonized. The carbonization of the as-prepared sample was further confirmed by Raman analysis (Fig. 2F). The characteristic peaks of carbon material appeared at  $\sim 1330\text{ cm}^{-1}$  (D band) and  $\sim 1584\text{ cm}^{-1}$  (G band) for Sn@NPC and pristine NPC.<sup>48,49</sup> The intensity ratio of  $I_D/I_G$  for Sn@NPC was calculated to be 0.97, possibly by virtue of the local deformation of the carbon material originating from Sn introduction, which was the reason for the increased  $I_D/I_G$  value of Sn@NPC compared to NPC ( $I_D/I_G = 0.86$ ). From the above results, it was verified that the Sn@NPC composites had been successfully synthesized on the bacterial template.

### 3.3 CO<sub>2</sub>RR activity and stability

The CO<sub>2</sub> electroreduction performances on NPC, Sn@NPC and Sn particles were systematically evaluated in a three-electrode H-type cell. Linear sweep voltammetry was first performed in 0.1 M KHCO<sub>3</sub> solution saturated with Ar or CO<sub>2</sub>. As shown in Fig. 3A, Sn particles and Sn@NPC obtained higher geometric current densities in CO<sub>2</sub>-saturated electrolyte than those in Ar-saturated electrolyte. The current density of Sn@NPC reached  $19.31\text{ mA cm}^{-2}$  at  $1.43\text{ V vs. RHE}$  and was higher than that of Sn particles ( $16.07\text{ mA cm}^{-2}$ ), which demonstrated that Sn@NPC exhibited higher selectivity for CO<sub>2</sub>RR. In contrast, there was no momentous diversity in the electrocatalytic activity of NPC under either Ar or CO<sub>2</sub>, indicating that the HER competition reaction dominated during the process. The main product of CO<sub>2</sub>

electrolysis was HCOOH as well as a small amount of CO. Clearly, the Sn@NPC displayed a higher current density for HCOOH production ( $j_{\text{HCOOH}}$ ) over the whole potential range when compared with Sn particles and NPC, and a large value of  $15.89\text{ mA cm}^{-2}$  could be obtained at  $1.43\text{ V vs. RHE}$  (Fig. 3B). To confirm the HCOOH was from CO<sub>2</sub> reduction, the liquid products in the Ar-purged system were analyzed, where a zero yield of HCOOH was detected (Fig. S6†). The distinct difference was that the new peak of HCOOH could be seen in CO<sub>2</sub>-saturated system, proving that the carbon source indeed originated from the purged CO<sub>2</sub> source.<sup>50</sup>

Moreover, we further quantified the reduction products at the selected potentials to assess the selectivity of these catalysts for CO<sub>2</sub>RR. As seen in Fig. 3C, the FE<sub>HCOOH</sub> of the Sn@NPC electrode could reach 61.46% even at a low applied potential of  $-0.6\text{ V vs. RHE}$ . As the potential increased to  $-1.05\text{ V vs. RHE}$ , the FE<sub>HCOOH</sub> reached as high as 87.93% and was associated with a stable  $j_{\text{HCOOH}}$  of  $-8.05\text{ mA cm}^{-2}$ , while the Sn particles revealed a maximum FE<sub>HCOOH</sub> of only 56.57% at a high bias of  $-1.1\text{ V vs. RHE}$  (Fig. 3D). Noteworthy, the FE<sub>HCOOH</sub> of Sn@NPC was stabilized at  $85 \pm 3\%$  over the wide potential range of  $-0.8$  to  $-1.3\text{ V vs. RHE}$ . In addition, when NPC was used as an electrocatalyst, the reduction products were mainly H<sub>2</sub> and a small amount of CO, and no HCOOH was detected (Fig. 3E). The above results confirmed that the Sn@NPC composites possessed outstanding activity and selectivity for CO<sub>2</sub>RR. For better figuring out the CO<sub>2</sub>RR performance difference, the ECSA-normalized current density of HCOOH was first calculated based on ECSA (Fig. S7†), which showed the highest current density of  $0.41\text{ mA cm}^{-2}$  at

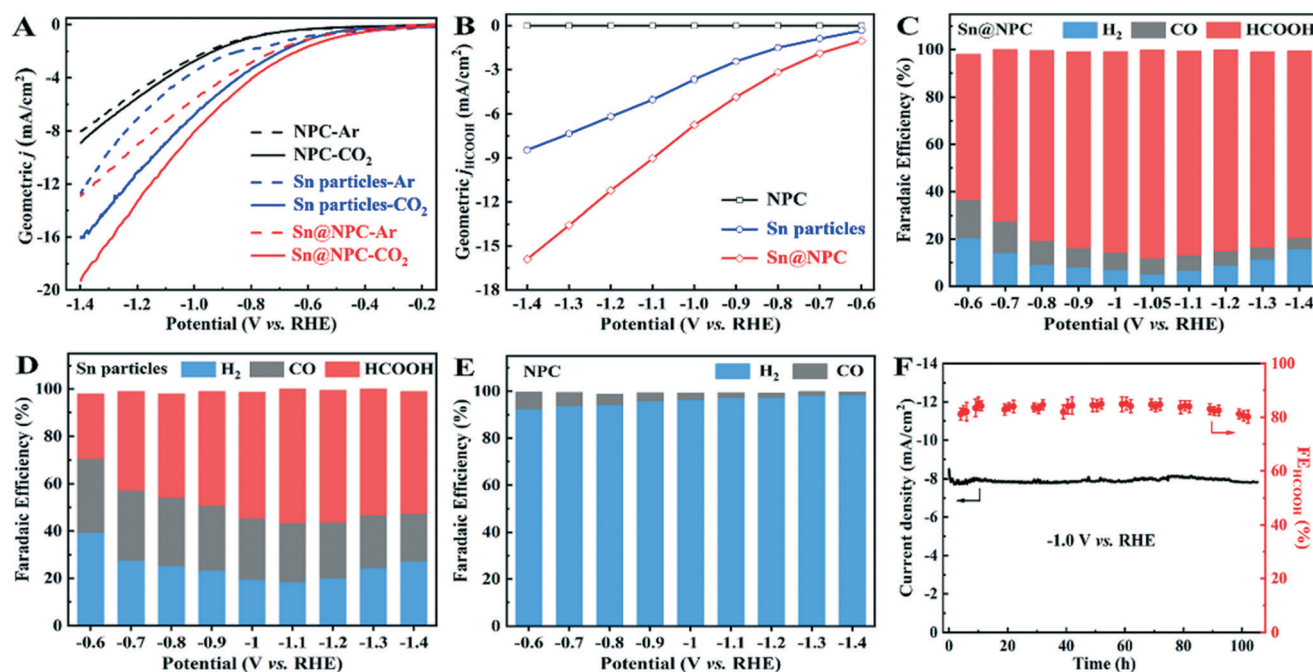


Fig. 3 CO<sub>2</sub>RR activity: (A) LSV curves and (B) calculated  $j_{\text{HCOOH}}$  values of NPC, Sn@NPC and Sn particles measured in CO<sub>2</sub>-saturated 0.1 M KHCO<sub>3</sub> aqueous solution; Faradaic efficiencies of the reduction products for (C) Sn@NPC, (D) Sn particles and (E) NPC in the range of all potentials; (F) long-term stability test of Sn@NPC at  $-1.0\text{ V vs. RHE}$ .

-1.4 V vs. RHE for the Sn@NPC electrode, almost 1.4 times higher than that of the Sn particles ( $0.3 \text{ mA cm}^{-2}$ ). Turnover frequencies were further calculated and the results are displayed in Fig. S8†. The Sn@NPC catalyst attained a TOF of  $419 \text{ h}^{-1}$  at -1.4 V vs. RHE, which was 13.5 times higher than that of the Sn particles ( $31 \text{ h}^{-1}$ ). These results showed that the Sn sites on the N/P-doped carbon had high efficiency for converting  $\text{CO}_2$  into HCOOH.

Stability is also critical for  $\text{CO}_2\text{RR}$  catalysts in practical application for evaluating the technical and economic feasibility. Therefore, a long-time electrolysis at -1.0 V vs. RHE was performed to evaluate the stability of the Sn@NPC electrode (Fig. 3F). Encouragingly, the Sn@NPC electrode exhibited a sustained  $\text{FE}_{\text{HCOOH}}$  of ~85% together with a current density of  $8 \text{ mA cm}^{-2}$  after operating for 105 h, which was superior to that of most Sn-based catalysts in similar systems (Table S4†). Moreover, there were no obvious changes in the morphology and crystal structure before and after the 105 h continuous testing (Fig. S9†), proving the excellent stability of the electrode. Also, the LSV curves of Sn@NPC also showed negligible changes after the stability test (Fig. S10†). In contrast, the  $\text{CO}_2\text{RR}$  activity of Sn particles showed an obvious degradation after 27 h electrolysis (Fig. S11†). All these results demonstrated that the Sn@NPC composites exhibited high activity and excellent stability for  $\text{CO}_2$  electroreduction to HCOOH, which could be ascribed to the uniform dispersion of the ultrafine Sn nanoparticles in the N/P-doped carbon (Fig. 1E).

### 3.4 Reaction kinetics and the role of N/P-doped carbon

To gain an insight into why Sn@NPC had such high  $\text{CO}_2\text{RR}$  performance, the electrochemical surface areas of the samples were first measured. The increase in ECSAs is one of the main reasons for the increased  $\text{CO}_2\text{RR}$  performance since a larger ECSA can provide more catalytically active sites.<sup>37,51</sup> Based on cyclic voltammetry at different scan rates (Fig. S12 and S13†), the ECSAs were estimated from the double-layer capacitance ( $C_{\text{dl}}$ ). As expected, Fig. 4A revealed a much larger value of  $38.9 \text{ cm}^2$  for Sn@NPC in comparison to those of the Sn particles ( $8.4 \text{ cm}^2$ ) and the bare NPC ( $2.9 \text{ cm}^2$ ), implying that the co-existence of Sn and N/P-doped carbon enhanced the electrochemically active sites. The reaction kinetic mechanism for the  $\text{CO}_2\text{RR}$  to HCOOH process was further elucidated by electrochemical impedance spectroscopy measurements and Tafel plots. As shown in Fig. 4B, the semicircle arc of the Sn@NPC electrode was much smaller than that of the Sn particles and NPC electrodes, implying that Sn@NPC had faster  $\text{CO}_2\text{RR}$  kinetics. The  $\text{CO}_2\text{RR}$  to HCOOH transfer kinetics was further quantitatively analyzed *via* fitting the EIS plots into an equivalent circuit model (Fig. S14†). Compared with the Sn particles ( $47.48 \text{ } \Omega$ ) and NPC electrodes ( $101.56 \text{ } \Omega$ ), the Sn@NPC electrode had a visibly reduced  $R_{\text{ct}}$  of  $36.04 \text{ } \Omega$  (Table S1†), evidencing the enhancement in charge transport during the  $\text{CO}_2\text{RR}$ , which was in agreement with its  $\text{CO}_2\text{RR}$  performance (*i.e.* the previous LSV curves). The Tafel analysis plots for  $\text{CO}_2$  reduction are shown in Fig. 4C, the Tafel slope of  $\text{H}_2$  at the

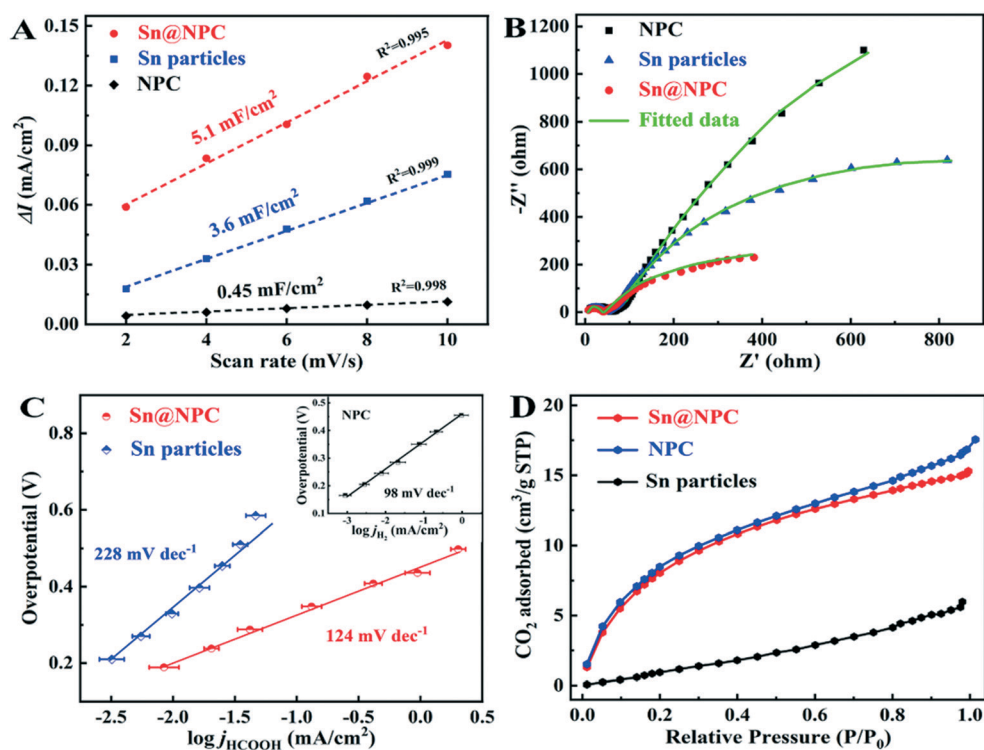


Fig. 4 (A) Charging current density differences plotted against scan rates; (B) Nyquist plots of the NPC, Sn@NPC and Sn particles catalysts; (C) Tafel plots and (D)  $\text{CO}_2$  adsorption isotherms.

NPC electrode was as low as  $98 \text{ mV dec}^{-1}$ , which was due to the fast kinetics towards  $\text{H}_2$  evolution on bare NPC metal. In contrast, the Tafel slope of  $\text{CO}_2\text{RR}$  to  $\text{HCOOH}$  was  $124 \text{ mV dec}^{-1}$  for the  $\text{Sn@NPC}$  electrode and was close to  $118 \text{ mV dec}^{-1}$ , suggesting the rate-limiting step is a single-electron-transfer process.<sup>21,52</sup> While the Tafel slope of Sn particles was  $228 \text{ mV dec}^{-1}$ , much higher than that of  $\text{Sn@NPC}$ , indicating a slower initial electron-transfer rate. Clearly, the above results demonstrated that the  $\text{Sn@NPC}$  electrocatalyst could kinetically promote the conversion of  $\text{CO}_2$  and enhance  $\text{HCOOH}$  selectivity.

The  $\text{CO}_2$ -adsorption capacity of the as-synthesized samples was also evaluated. It is generally accepted that a high  $\text{CO}_2$ -adsorption capacity on an electrocatalyst surface can supply sufficient base material to sustain the following reaction.<sup>7</sup> The results in Fig. 4D showed that the  $\text{CO}_2$ -adsorption capacity of NPC and  $\text{Sn@NPC}$  could reach 17.6 and 15.3

$\text{cm}^3 \text{ g}^{-1}$  at 1.0 atm, respectively. In comparison with Sn particles ( $5.9 \text{ cm}^3 \text{ g}^{-1}$  at 1.0 atm), the  $\text{CO}_2$ -adsorption capacity was increased by about two times, indicating that N/P-doped carbon could promote  $\text{CO}_2$  adsorption. Further, we calculated the adsorption energies of  $\text{CO}_2$  on N/P-doped graphene, and bare Sn sites of (101), (200) and the adsorption structures are given in Fig. S15 and S16.† Compared to bare graphene ( $-0.245 \text{ eV}$ ), the doped system showed a significantly enhanced adsorption of  $\text{CO}_2$  (pyridine nitrogen, graphite nitrogen, pyrrole nitrogen were  $-1.79$ ,  $-1.85$  and  $-1.83 \text{ eV}$ , respectively), indicating that the introduction of N could intensify the adsorption of  $\text{CO}_2$ . In other words, the vicinity or surface of Sn in  $\text{Sn@NPC}$  could construct a  $\text{CO}_2$ -rich condition, which can then continuously provide raw materials for subsequent  $\text{CO}_2\text{RR}$ . According to the major Sn surfaces (Fig. 2A), the adsorption energies of  $\text{CO}_2$  for Sn(101) and Sn(200) surfaces were  $-0.28$  and  $-0.33 \text{ eV}$ , respectively.

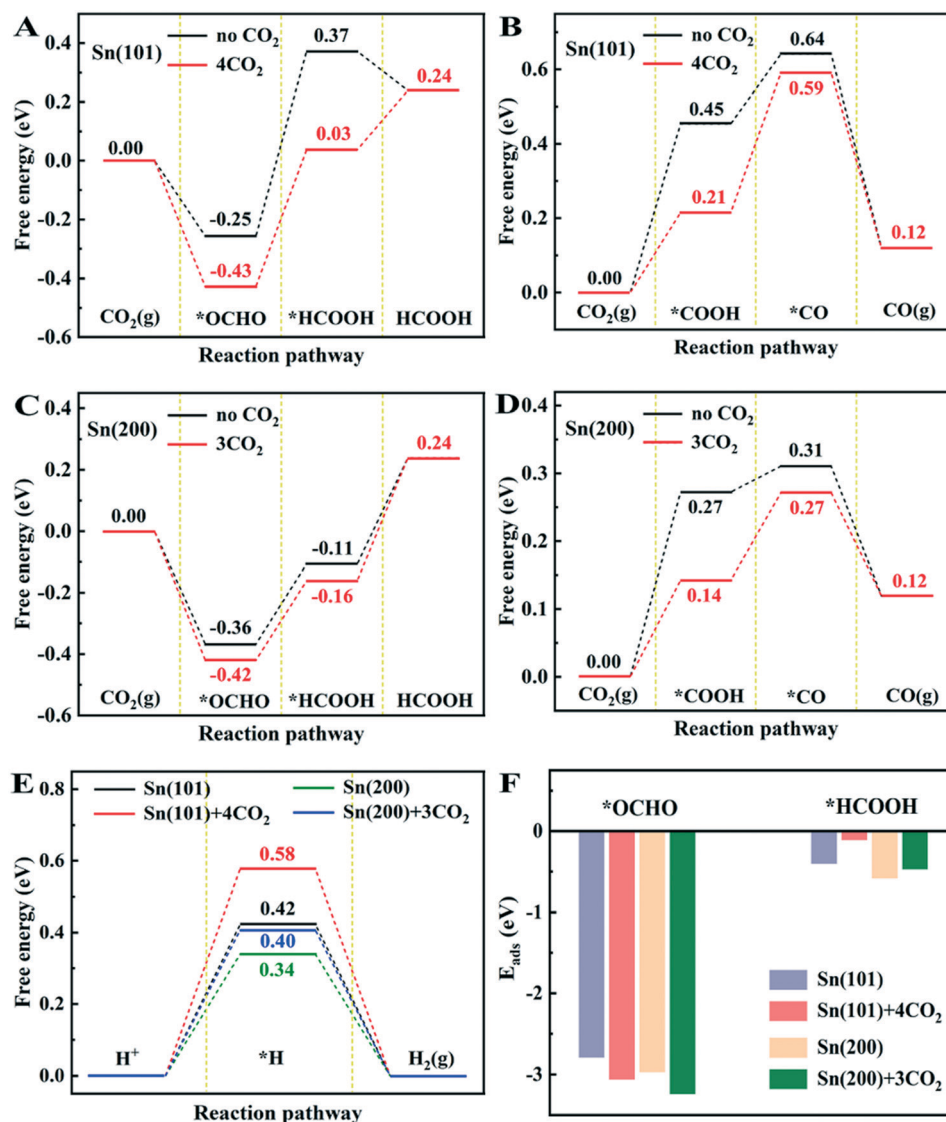


Fig. 5 DFT calculations: (A–E) DFT investigation results of the calculated free-energy diagram; (F) adsorption energy of  $\text{*OCHO}$  and  $\text{*HCOOH}$  species.

When under CO<sub>2</sub>-enriched conditions, the adsorption of CO<sub>2</sub> by Sn(101) and Sn(200) surfaces (−0.29 eV and −0.45 eV) was significantly enhanced. This was consistent with the experimental results, in which Sn@NPC had the best CO<sub>2</sub>RR to HCOOH activity, superior to Sn particles and NPC under the same conditions.

### 3.5 DFT calculation and reaction mechanism

According to the above studies, the excellent CO<sub>2</sub>RR performance of Sn@NPC composites could be attributed to the co-existence of ultrafine Sn nanoparticles and N/P-doped carbon. DFT calculations were then performed to further elucidate the key to the outstanding CO<sub>2</sub>RR performance of Sn@NPC. As presented in Fig. 5, the CO<sub>2</sub>-reduction process involved three competing reactions in our experiment, with the potential-limiting steps being the formation of \*OCHO, \*COOH and \*H. Compared to Fig. 5A and C, the Gibbs free energies of the \*OCHO intermediate on the CO<sub>2</sub>-rich Sn(101) and Sn(200) surfaces were 0.18 and 0.06 eV higher than those without any molecular CO<sub>2</sub>, proving that the CO<sub>2</sub>-rich Sn(101) and Sn(200) surfaces could accelerate the formation of \*OCHO. Noteworthy, the free energy of the \*COOH intermediate also decreased significantly when enriched with CO<sub>2</sub> on the Sn(101) and Sn(200) surfaces (Fig. 5B and D and S17†), which was regarded as the indispensable step for CO formation. However, the free energy of the \*CO intermediate was higher than that of the \*COOH and \*HCOOH intermediates for both Sn(101) and Sn(200) (Fig. S18†). Thus, CO formation would be suppressed at the Sn surface. The \*COOH intermediate has the possibility to generate the \*HCOOH intermediate because of the lower free energy of \*HCOOH. In fact, the Gibbs free energy of formation for \*OCHO was lower than that of \*COOH and \*H. Therefore, the CO<sub>2</sub>RR to HCOOH reaction occurring on the Sn surface could be attributed to the energetic feasibility of \*OCHO rather than \*COOH, and this conclusion was also confirmed by the subsequent *in situ* Raman spectra. On the other hand, we noted that the free energy of the \*H intermediate increased instead of that on the CO<sub>2</sub>-rich Sn(101) and Sn(200) surfaces, indicating the further inhibition of H<sub>2</sub> production (Fig. 5E). As a result, the best CO<sub>2</sub>RR to HCOOH performance could be achieved on Sn@NPC due to the rich CO<sub>2</sub> content. Furthermore, the adsorption energies of the \*OCHO and \*HCOOH intermediates under various conditions were calculated. As displayed in Fig. 5F, the adsorption energy of \*OCHO became stronger on the CO<sub>2</sub>-rich Sn(101) surface (−3.06 eV) than on the Sn(101) surface (−2.79 eV), and a similar result was presented for the Sn(200) surface (Fig. S19†). Satisfyingly, the adsorption energies of \*HCOOH on the CO<sub>2</sub>-rich Sn(101) and Sn(200) surfaces (−0.11 and −0.47 eV) were clearly lower than those without CO<sub>2</sub> (−0.40 and −0.58 eV) (Fig. S20†). The weaker \*HCOOH adsorption energy demonstrated that HCOOH was more easily desorbed from the surface of the Sn@NPC electrode. Reviewing the above electrochemical studies, the broader potential window

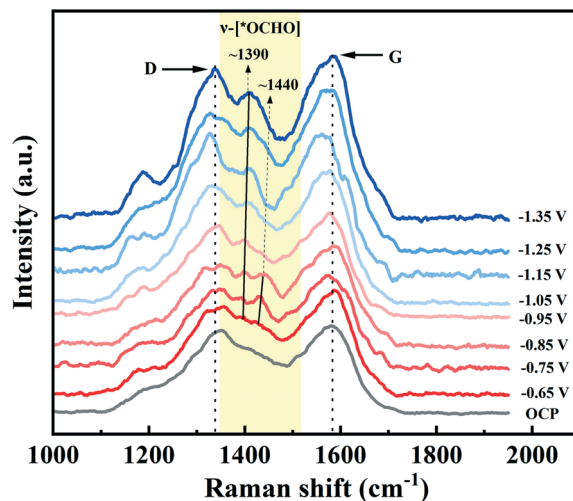


Fig. 6 Electrochemical *in situ* Raman spectra results on Sn@NPC at various applied potential (vs. SCE reference electrode).

selectivity and the long-time durability for CO<sub>2</sub>RR to HCOOH could be interpreted as due to the enriched CO<sub>2</sub> concentration, the enhanced \*OCHO adsorption and the weakened \*HCOOH adsorption on the Sn@NPC electrode.

To verify the above experimental and DFT calculation results, we further performed *in situ* electrochemical Raman characterization in CO<sub>2</sub>-saturated 0.1 M KHCO<sub>3</sub> electrolyte, which is known to be an effective tool to real-time monitor the intermediate species adsorbed on a catalyst surface during the CO<sub>2</sub> reduction process.<sup>53,54</sup> From Fig. 6, strong-band and weak-band peaks arising at ~1390 and ~1440 cm<sup>−1</sup> were observed on Sn@NPC electrode, which could be attributed to the symmetric stretching vibration of O-bound bidentate \*OCHO species (an intermediate to HCOOH).<sup>54,55</sup> The intensity of the peak at ~1390 cm<sup>−1</sup> increased with the increment of the applied cathode potential, implying an increasing surface coverage of \*OCHO species. In contrast, no signals belonging to \*OCHO intermediates was found at the open circuit potential (OCP). This result demonstrated the superior \*OCHO binding ability on the Sn@NPC electrode surface, thus boosting the performance of the CO<sub>2</sub>-RR to HCOOH, which was in agreement with the obtained DFT calculations as well the experimental results above.

## 4. Conclusions

In summary, we put forward an ideal material model of ultrafine Sn nanoparticles homogeneously distributed on N/P-doped carbon, by upcycling the Sn metal from electroplating sludge using bacteria. CO<sub>2</sub>-adsorption analysis and DFT calculations demonstrated that the N/P-doped carbon could enhance CO<sub>2</sub> adsorption, which could provide sufficient CO<sub>2</sub> to the catalyst, which then efficiently promoted the \*OCHO intermediate generation and prevented the association of protons for the hydrogen evolution. Moreover, DFT calculations and *in situ* Raman characterization proved

that there were stronger adsorption of the \*OCHO intermediate and weaker adsorption of \*HCOOH on the CO<sub>2</sub>-rich Sn(101) and Sn(200) surfaces. Thus, a maximum HCOOH selectivity of 87.93% at 1.05 V vs. RHE was observed on the Sn@NPC electrode, which kept an FE<sub>HCOOH</sub> of over 80% within a 500 mV wide potential window. In addition, the outstanding CO<sub>2</sub>RR-to-HCOOH performance of the Sn@NPC electrode was also reflected in the strong stability with a stable FE<sub>HCOOH</sub> (~85%) and current density (~8.0 mA/cm<sup>2</sup>) over 105 h at 1.0 V vs. RHE. This study may offer a strategy for recycling the metal from electroplating sludge, allowing the large-scale preparation of high-performance electrocatalysts with wide applications in the CO<sub>2</sub>RR.

## Author contributions

Xiaohui Zhong: conceptualization, methodology, formal analysis, investigation, writing – original draft. Zuqi Zhong, Shujie Liang and Gongchang Zeng: formal analysis, writing – review & editing. Shuang Cheng: resources. Hong Deng and Zhang Lin: conceptualization, writing – review & editing, supervision, validation, project administration, funding acquisition.

## Conflicts of interest

The authors declare that there is no conflict of interest.

## Acknowledgements

This work was financially supported by the National Natural Science Foundation of China (No. 21777046), the National Key Research and Development Program of China (No. 2019YFA1805902 and 2019YFA0210402), and the Guangdong Science and Technology Program (2020B121201003).

## References

- Z. Huang, R. G. Grim, J. A. Schaidle and L. Tao, The economic outlook for converting CO<sub>2</sub> and electrons to molecules, *Energy Environ. Sci.*, 2021, **14**, 3664–3678.
- S. Gao, Y. Lin, X. Jiao, Y. Sun, Q. Luo, W. Zhang, D. Li, J. Yang and Y. Xie, Partially oxidized atomic cobalt layers for carbon dioxide electroreduction to liquid fuel, *Nature*, 2016, **529**, 68–71.
- A. K. Singh, J. H. Montoya, J. M. Gregoire and K. A. Persson, Robust and synthesizable photocatalysts for CO<sub>2</sub> reduction: a data-driven materials discovery, *Nat. Commun.*, 2019, **10**, 443.
- S. Liang, B. Han, X. Qu, X. Ye, W. Chen, H. Deng, C. Tian and Z. Lin, Lattice-strained nickel hydroxide nanosheets for the boosted diluted CO<sub>2</sub> photoreduction, *Environ. Sci.: Nano*, 2021, **8**, 2360–2371.
- B. M. Tackett, E. Gomez and J. G. Chen, Net reduction of CO<sub>2</sub> via its thermocatalytic and electrocatalytic transformation reactions in standard and hybrid processes, *Nat. Catal.*, 2019, **2**, 381–386.
- J. Feng, J. Ni and H. Pan, Synergistic carbon and hydrogen reactions in the electrochemical reduction of CO<sub>2</sub> to liquid fuels, *J. Mater. Chem. A*, 2021, **9**, 10546–10561.
- G. Wang, J. Chen, Y. Ding, P. Cai, L. Yi, Y. Li, C. Tu, Y. Hou, Z. Wen and L. Dai, Electrocatalysis for CO<sub>2</sub> conversion: from fundamentals to value-added products, *Chem. Soc. Rev.*, 2021, **50**, 4993–5061.
- C. Long, X. Li, J. Guo, Y. Shi, S. Liu and Z. Tang, Electrochemical reduction of CO<sub>2</sub> over heterogeneous catalysts in aqueous solution: Recent progress and perspectives, *Small Methods*, 2018, **3**, 1800369.
- R. B. Song, W. Zhu, J. Fu, Y. Chen, L. Liu, J. R. Zhang, Y. Lin and J. J. Zhu, Electrode materials engineering in electrocatalytic CO<sub>2</sub> reduction: Energy input and conversion efficiency, *Adv. Mater.*, 2020, **32**, 1903796.
- N. Han, P. Ding, L. He, Y. Li and Y. Li, Promises of main group metal-based nanostructured materials for electrochemical CO<sub>2</sub> reduction to formate, *Adv. Energy Mater.*, 2019, **10**, 1902338.
- P. Ding, H. Zhao, T. Li, Y. Luo, G. Fan, G. Chen, S. Gao, X. Shi, S. Lu and X. Sun, Metal-based electrocatalytic conversion of CO<sub>2</sub> to formic acid/formate, *J. Mater. Chem. A*, 2020, **8**, 21947–21960.
- M. Alfath and C. W. Lee, Recent advances in the catalyst design and mass transport control for the electrochemical reduction of carbon dioxide to formate, *Catalysts*, 2020, **10**, 859.
- Y. Wang, C. Li, Z. Fan, Y. Chen, X. Li, L. Cao, C. Wang, L. Wang, D. Su, H. Zhang, T. Mueller and C. Wang, Undercoordinated active sites on 4H gold nanostructures for CO<sub>2</sub> reduction, *Nano Lett.*, 2020, **20**, 8074–8080.
- W. Zhu, Y. J. Zhang, H. Zhang, H. Lv, Q. Li, R. Michalsky, A. A. Peterson and S. Sun, Active and selective conversion of CO<sub>2</sub> to CO on ultrathin Au nanowires, *J. Am. Chem. Soc.*, 2014, **136**, 16132–16135.
- Z. Zhang, G. Wen, D. Luo, B. Ren, Y. Zhu, R. Gao, H. Dou, G. Sun, M. Feng, Z. Bai, A. Yu and Z. Chen, “Two ships in a bottle” design for Zn-Ag-O catalyst enabling selective and long-lasting CO<sub>2</sub> electroreduction, *J. Am. Chem. Soc.*, 2021, **143**, 6855–6864.
- S. Lamaison, D. Wakerley, J. Blanchard, D. Montero, G. Rousse, D. Mercier, P. Marcus, D. Taverna, D. Giaume, V. Mougél and M. Fontecave, High-current-density CO<sub>2</sub>-to-CO electroreduction on Ag-alloyed Zn dendrites at elevated pressure, *Joule*, 2020, **4**, 395–406.
- X. Sun, Y. Tuo, C. Ye, C. Chen, Q. Lu, G. Li, P. Jiang, S. Chen, P. Zhu, M. Ma, J. Zhang, J. H. Bitter, D. Wang and Y. Li, Phosphorus induced electron localization of single iron sites for boosted CO<sub>2</sub> electroreduction reaction, *Angew. Chem., Int. Ed.*, 2021, **60**, 23614–23618.
- N. Zhang, X. Zhang, Y. Kang, C. Ye, R. Jin, H. Yan, R. Lin, J. Yang, Q. Xu, Y. Wang, Q. Zhang, L. Gu, L. Liu, W. Song, J. Liu, D. Wang and Y. Li, A supported Pd<sub>2</sub> dual-atom site catalyst for efficient electrochemical CO<sub>2</sub> reduction, *Angew. Chem., Int. Ed.*, 2021, **60**, 13388–13393.
- J. Wu, X. Bai, Z. Ren, S. Du, Z. Song, L. Zhao, B. Liu, G. Wang and H. Fu, Multivalent Sn species synergistically

- favours the CO<sub>2</sub>-into-HCOOH conversion, *Nano Res.*, 2021, **14**, 1053–1060.
- 20 Z. Chen, T. Fan, Y.-Q. Zhang, J. Xiao, M. Gao, N. Duan, J. Zhang, J. Li, Q. Liu, X. Yi and J.-L. Luo, Wavy SnO<sub>2</sub> catalyzed simultaneous reinforcement of carbon dioxide adsorption and activation towards electrochemical conversion of CO<sub>2</sub> to HCOOH, *Appl. Catal., B*, 2020, **261**, 118243.
  - 21 P. Deng, H. Wang, R. Qi, J. Zhu, S. Chen, F. Yang, L. Zhou, K. Qi, H. Liu and B. Y. Xia, Bismuth oxides with enhanced bismuth-oxygen structure for efficient electrochemical reduction of carbon dioxide to formate, *ACS Catal.*, 2019, **10**, 743–750.
  - 22 J. Liu, Y. Li, Y. Wang, C. Xiao, M. Liu, X. Zhou, H. Jiang and C. Li, Isolated ultrasmall Bi nanosheets for efficient CO<sub>2</sub>-to-formate electroreduction, *Nano Res.*, 2021, 1–6.
  - 23 S. Back, J. H. Kim, Y. T. Kim and Y. Jung, On the mechanism of high product selectivity for HCOOH using Pb in CO<sub>2</sub> electroreduction, *Phys. Chem. Chem. Phys.*, 2016, **18**, 9652–9657.
  - 24 J. E. Pander, J. W. J. Lum and B. S. Yeo, The importance of morphology on the activity of lead cathodes for the reduction of carbon dioxide to formate, *J. Mater. Chem. A*, 2019, **7**, 4093–4101.
  - 25 R. Hegner, L. F. M. Rosa and F. Harnisch, Electrochemical CO<sub>2</sub> reduction to formate at indium electrodes with high efficiency and selectivity in pH neutral electrolytes, *Appl. Catal., B*, 2018, **238**, 546–556.
  - 26 W. Luo, W. Xie, M. Li, J. Zhang and A. Züttel, 3D hierarchical porous indium catalyst for highly efficient electroreduction of CO<sub>2</sub>, *J. Mater. Chem. A*, 2019, **7**, 4505–4515.
  - 27 Y. Zhou, R. Zhou, X. Zhu, N. Han, B. Song, T. Liu, G. Hu, Y. Li, J. Lu and Y. Li, Mesoporous PdAg nanospheres for stable electrochemical CO<sub>2</sub> reduction to formate, *Adv. Mater.*, 2020, **32**, 2000992.
  - 28 B. Jiang, X. G. Zhang, K. Jiang, D. Y. Wu and W. B. Cai, Boosting formate production in electrocatalytic CO<sub>2</sub> reduction over wide potential window on Pd surfaces, *J. Am. Chem. Soc.*, 2018, **140**, 2880–2889.
  - 29 S. Zhang, P. Kang, S. Ubnoske, M. K. Brennaman, N. Song, R. L. House, J. T. Glass and T. J. Meyer, Polyethylenimine-enhanced electrocatalytic reduction of CO<sub>2</sub> to formate at nitrogen-doped carbon nanomaterials, *J. Am. Chem. Soc.*, 2014, **136**, 7845–7848.
  - 30 Y. Liu, J. Zhao and Q. Cai, Pyrrolic-nitrogen doped graphene: a metal-free electrocatalyst with high efficiency and selectivity for the reduction of carbon dioxide to formic acid: a computational study, *Phys. Chem. Chem. Phys.*, 2016, **18**, 5491–5498.
  - 31 Y. Hori, H. Wakebe, T. Tsukamoto and O. Koga, Electrocatalytic process of CO selectivity in electrochemical reduction of CO<sub>2</sub> at metal electrodes in aqueous media, *Electrochim. Acta*, 1994, **39**, 1833–1839.
  - 32 B. Kumar, V. Atla, J. P. Brian, S. Kumari, T. Q. Nguyen, M. Sunkara and J. M. Spurgeon, Reduced SnO<sub>2</sub> porous nanowires with a high density of grain boundaries as catalysts for efficient electrochemical CO<sub>2</sub>-into-HCOOH conversion, *Angew. Chem., Int. Ed.*, 2017, **56**, 3645–3649.
  - 33 C. Zhao and J. Wang, Electrochemical reduction of CO<sub>2</sub> to formate in aqueous solution using electro-deposited Sn catalysts, *Chem. Eng. J.*, 2016, **293**, 161–170.
  - 34 F. Li, L. Chen, M. Xue, T. Williams, Y. Zhang, D. R. MacFarlane and J. Zhang, Towards a better Sn: Efficient electrocatalytic reduction of CO<sub>2</sub> to formate by Sn/SnS<sub>2</sub> derived from SnS<sub>2</sub> nanosheets, *Nano Energy*, 2017, **31**, 270–277.
  - 35 F. Lei, W. Liu, Y. Sun, J. Xu, K. Liu, L. Liang, T. Yao, B. Pan, S. Wei and Y. Xie, Metallic tin quantum sheets confined in graphene toward high-efficiency carbon dioxide electroreduction, *Nat. Commun.*, 2016, **7**, 12697.
  - 36 T. Tsujiguchi, Y. Kawabe, S. Jeong, T. Ohto, S. Kukunuri, H. Kuramochi, Y. Takahashi, T. Nishiuchi, H. Masuda, M. Wakisaka, K. Hu, G. Elumalai, J.-I. Fujita and Y. Ito, Acceleration of electrochemical CO<sub>2</sub> reduction to formate at the Sn/reduced graphene oxide interface, *ACS Catal.*, 2021, **11**, 3310–3318.
  - 37 A. Mahsud, J. Chen, X. Yuan, F. Lyu, Q. Zhong, J. Chen, Y. Yin and Q. Zhang, Self-templated formation of cobalt-embedded hollow N-doped carbon spheres for efficient oxygen reduction, *Nano Res.*, 2021, **14**, 2819–2825.
  - 38 P. Iyengar, J. Huang, G. L. De Gregorio, C. Gadiyar and R. Buonsanti, Size dependent selectivity of Cu nano-octahedra catalysts for the electrochemical reduction of CO<sub>2</sub> to CH<sub>4</sub>, *Chem. Commun.*, 2019, **55**, 8796–8799.
  - 39 F. Ning, M. Shao, S. Xu, Y. Fu, R. Zhang, M. Wei, D. G. Evans and X. Duan, TiO<sub>2</sub>/graphene/NiFe-layered double hydroxide nanorod array photoanodes for efficient photoelectrochemical water splitting, *Energy Environ. Sci.*, 2016, **9**, 2633–2643.
  - 40 D. Yang, H. Yu, T. He, S. Zuo, X. Liu, H. Yang, B. Ni, H. Li, L. Gu, D. Wang and X. Wang, Visible-light-switched electron transfer over single porphyrin-metal atom center for highly selective electroreduction of carbon dioxide, *Nat. Commun.*, 2019, **10**, 3844.
  - 41 Y. Xing, X. Kong, X. Guo, Y. Liu, Q. Li, Y. Zhang, Y. Sheng, X. Yang, Z. Geng and J. Zeng, Bi@Sn core-shell structure with compressive strain boosts the electroreduction of CO<sub>2</sub> into formic acid, *Adv. Sci.*, 2020, **7**, 1902989.
  - 42 J. Gu, F. Heroguel, J. Luterbacher and X. Hu, Densely packed, Ultra small SnO nanoparticles for enhanced activity and selectivity in electrochemical CO<sub>2</sub> reduction, *Angew. Chem., Int. Ed.*, 2018, **57**, 2943–2947.
  - 43 J. Huang, Y. Sun, Y. Zhang, G. Zou, C. Yan, S. Cong, T. Lei, X. Dai, J. Guo, R. Lu, Y. Li and J. Xiong, A new member of electrocatalysts based on nickel metaphosphate nanocrystals for efficient water oxidation, *Adv. Mater.*, 2018, **30**, 1705045.
  - 44 D. Guo, R. Shibuya, C. Akiba, S. Saji, T. Kondo and J. Nakamura, Active sites of nitrogen-doped carbon materials for oxygen reduction reaction clarified using model catalysts, *Science*, 2016, **351**, 361–365.
  - 45 Q. Dong, H. Su, W. Cao, D. Zhang, Q. Guo and F. Zhang, Assembly and formation of biomorphic tin dioxide by a biomimetic sol-gel approach involving glycoprotein, *Eur. J. Inorg. Chem.*, 2007, **2007**, 2265–2273.

- 46 X. Ye, Z. Lin, S. Liang, X. Huang, X. Qiu, Y. Qiu, X. Liu, D. Xie, H. Deng, X. Xiong and Z. Lin, Upcycling of electroplating sludge into ultrafine Sn@C nanorods with highly stable lithium storage performance, *Nano Lett.*, 2019, **19**, 1860–1866.
- 47 A. H. Lim, H. W. Shim, S. D. Seo, G. H. Lee, K. S. Park and D. W. Kim, Biomineralized Sn-based multiphase nanostructures for Li-ion battery electrodes, *Nanoscale*, 2012, **4**, 4694–4701.
- 48 X. Zhao, H. Wan, P. Liang, N. Wang, C. Wang, Y. Gan, X. Chen, Q. Tan, X. Liu, J. Zhang, Y. Wang, H. Wang and H. Wang, Favorable anion adsorption/desorption of high rate NiSe<sub>2</sub> nanosheets/hollow mesoporous carbon for battery-supercapacitor hybrid devices, *Nano Res.*, 2021, **14**, 2574–2583.
- 49 P. Su, W. Huang, J. Zhang, U. Guharoy, Q. Du, Q. Sun, O. Jiang, Y. Cheng, J. Yang, X. Zhang, Y. Liu, S. P. Jiang and J. Liu, Fe atoms anchored on defective nitrogen doped hollow carbon spheres as efficient electrocatalysts for oxygen reduction reaction, *Nano Res.*, 2021, **14**, 1069–1077.
- 50 J. Y. Kim, W. Park, C. Choi, G. Kim, K. M. Cho, J. Lim, S. J. Kim, A. Al-Saggaf, I. Gereige, H. Lee, W.-B. Jung, Y. Jung and H.-T. Jung, High facets on nanowrinkled Cu via chemical vapor deposition graphene growth for efficient CO<sub>2</sub> reduction into ethanol, *ACS Catal.*, 2021, **11**, 5658–5665.
- 51 X. Ma, J. Du, H. Sun, F. Ye, X. Wang, P. Xu, C. Hu, L. Zhang and D. Liu, Boron, nitrogen co-doped carbon with abundant mesopores for efficient CO<sub>2</sub> electroreduction, *Appl. Catal., B*, 2021, **298**, 120543.
- 52 H. Wang, Y. Chen, X. Hou, C. Ma and T. Tan, Nitrogen-doped graphenes as efficient electrocatalysts for the selective reduction of carbon dioxide to formate in aqueous solution, *Green Chem.*, 2016, **18**, 3250–3256.
- 53 Z. Tao, Z. Wu, Y. Wu and H. Wang, Activating copper for electrocatalytic CO<sub>2</sub> reduction to formate via molecular interactions, *ACS Catal.*, 2020, **10**, 9271–9275.
- 54 D. Bohra, I. Ledezma-Yanez, G. Li, W. de Jong, E. A. Pidko and W. A. Smith, Lateral adsorbate interactions inhibit HCOO<sup>-</sup> while promoting CO selectivity for CO<sub>2</sub> electrocatalysis on silver, *Angew. Chem., Int. Ed.*, 2019, **58**, 1345–1349.
- 55 H. Liu, Y. Su, S. Kuang, E. J. M. Hensen, S. Zhang and X. Ma, Highly efficient CO<sub>2</sub> electrolysis within a wide operation window using octahedral tin oxide single crystals, *J. Mater. Chem. A*, 2021, **9**, 7848–7856.